Supporting Information

A High-Efficiency Ammonia-Responsive Solar Evaporator

Jingjing Xing,[‡,a] Jintao Tong,[‡,a] Ye Liu,[a] Yutong Guo,[a] Lanjian Zhuge,[c] Dafeng Zhang,[d] Ruomeng Duan,[e] Bo Song,[b] Yu Zhao,[a] Bin Dong[,a]*

[a]Institute of Functional Nano & Soft Materials (FUNSOM), Jiangsu Key Laboratory for Carbon-Based Functional Materials & Devices, Soochow University, Suzhou, Jiangsu 215123, PR China.

[b]Laboratory of Advanced Optoelectronic Materials, College of Chemistry, Chemical Engineering and Materials Science, Soochow University, Suzhou, Jiangsu 215123, China

[c]College of Physics, Soochow University, Suzhou, Jiangsu 215006, China

[d]School of Materials Science and Engineering, Liaocheng University, Liaocheng, Shandong, 252000, P. R. China

[e]School of Environment and Civil Engineering, Dongguan University of Technology, Dongguan, 523808, P. R. China

[‡]These authors contribute equally to this work.

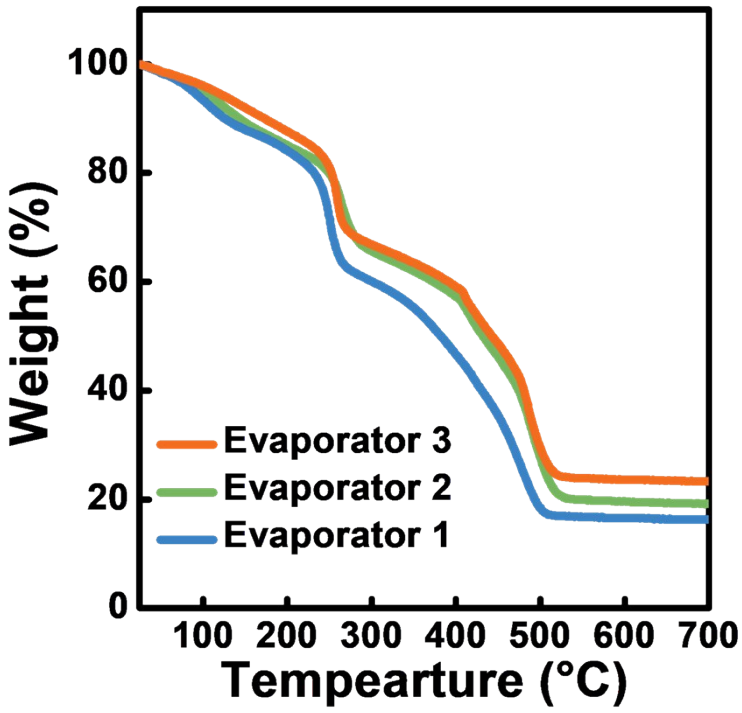

Fig. S1 TGA of the TiO_2/PPyNP based solar evaporators. The contents of TiO_2 are 15 wt% (blue line, denoted as evaporator 1), 20 wt% (green line, denoted as evaporator 2) and 25 wt% (red line, denoted as evaporator 3).

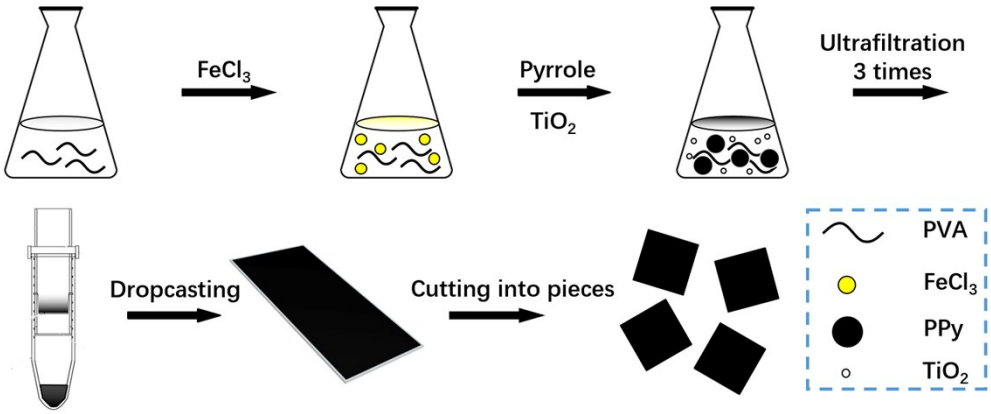

Fig. S2 Schematic illustration showing the synthesis process of the TiO_2/PPyNP based solar evaporator.

Numerical simulation

The simulation was conducted by COMSOL Multiphysics based on a model which showed the porous structure as shown in Fig. 3c. The heat transfer in the membrane could be described by the following equation according to the literature [1]:

$$E_{in} = \rho C_p \frac{\partial T(x,t)}{\partial t} + \rho C_p v \nabla T(x,t) + \nabla[k \nabla T(x,t)]$$

where E_{in} represents the thermal energy input from the photothermal conversion. ρ, C_p and T are mass density, liquid heat capacity and local temperature, respectively; ν and k are fluid flow velocity and thermal conductivity of the aqueous medium. The ambient temperature and water temperature were set to 298 k.

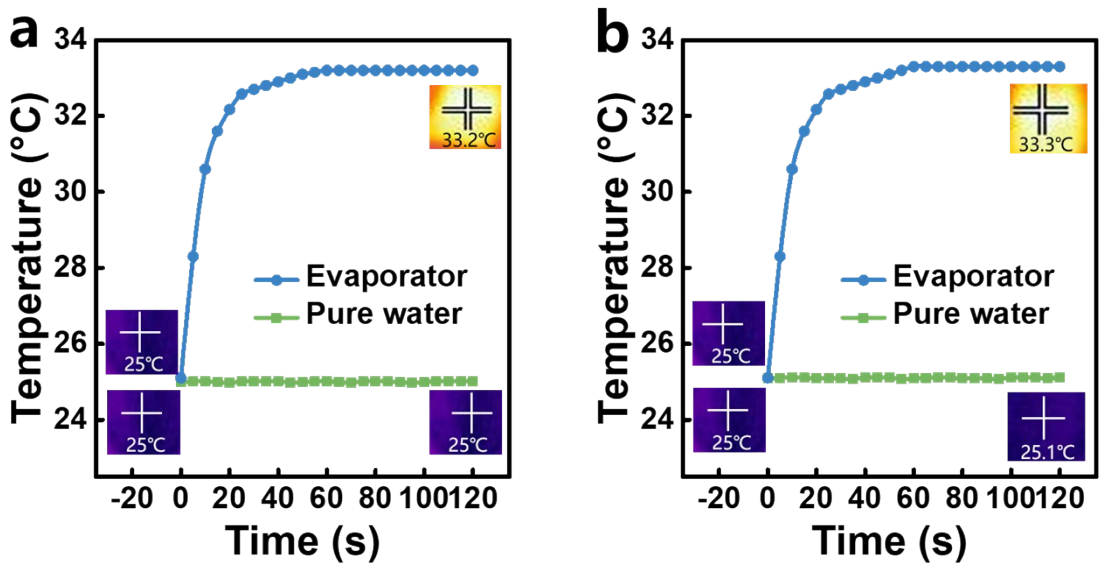

Fig. S3 Under 2 sun irradiation, the changes in the temperature of the bulk water (green curves) and solar evaporator (blue curves) on (a) lake water and (b) seawater. Insets: FLIR images showing the initial and final temperatures, respectively.

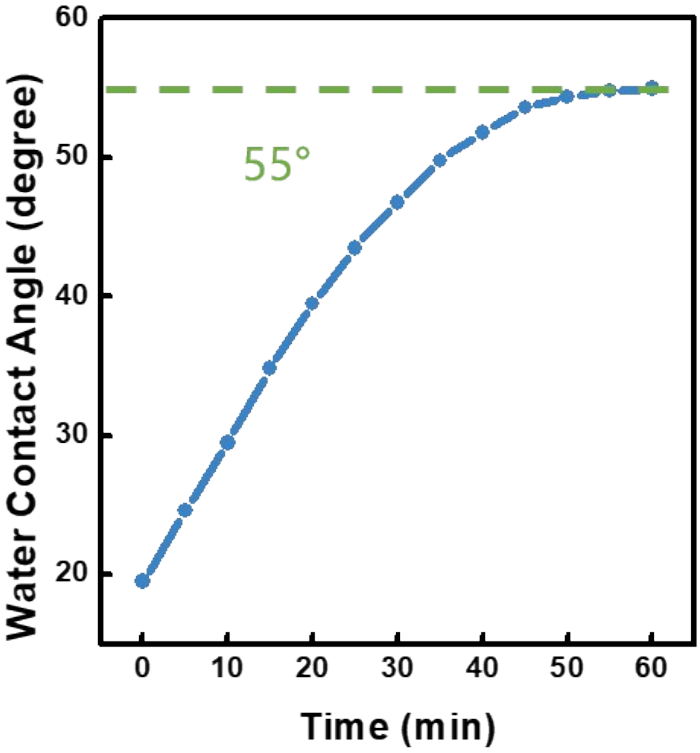

Fig. S4 The contact angle of the evaporator changes back to the original value within 1 h after removing the light source.

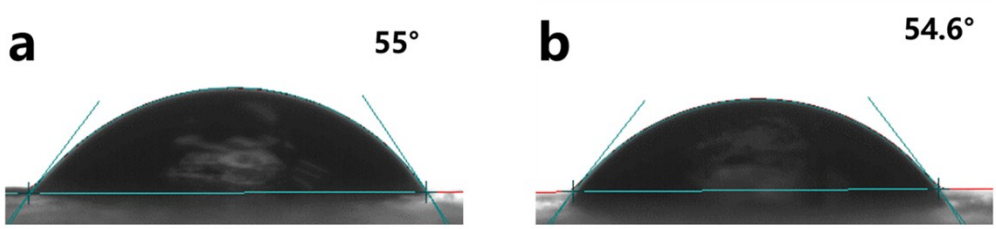

Fig. S5 The contact angle of the evaporator surface (a) before and (b) after heating at 34 ˚C.

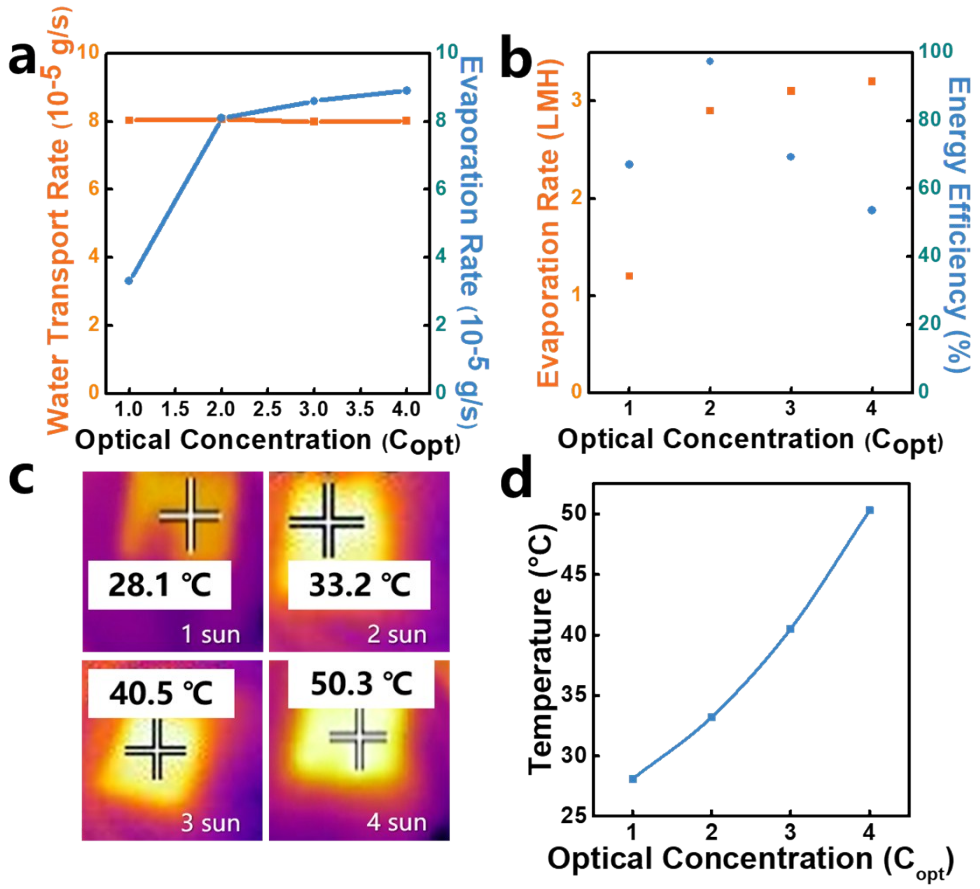

Fig. S6 (a) The water transport rates and the evaporation rates of the evaporator under solar irradiation with different optical concentration. (b) The evaporation rates and the energy efficiencies of the evaporator under different solar irradiation conditions. (c) The FLIR images of the solar evaporator under 1, 2, 3 and 4 sun irradiation for 2 min. (d) The relationship between temperature of solar evaporator and optical concentration (irradiated for 2 min).

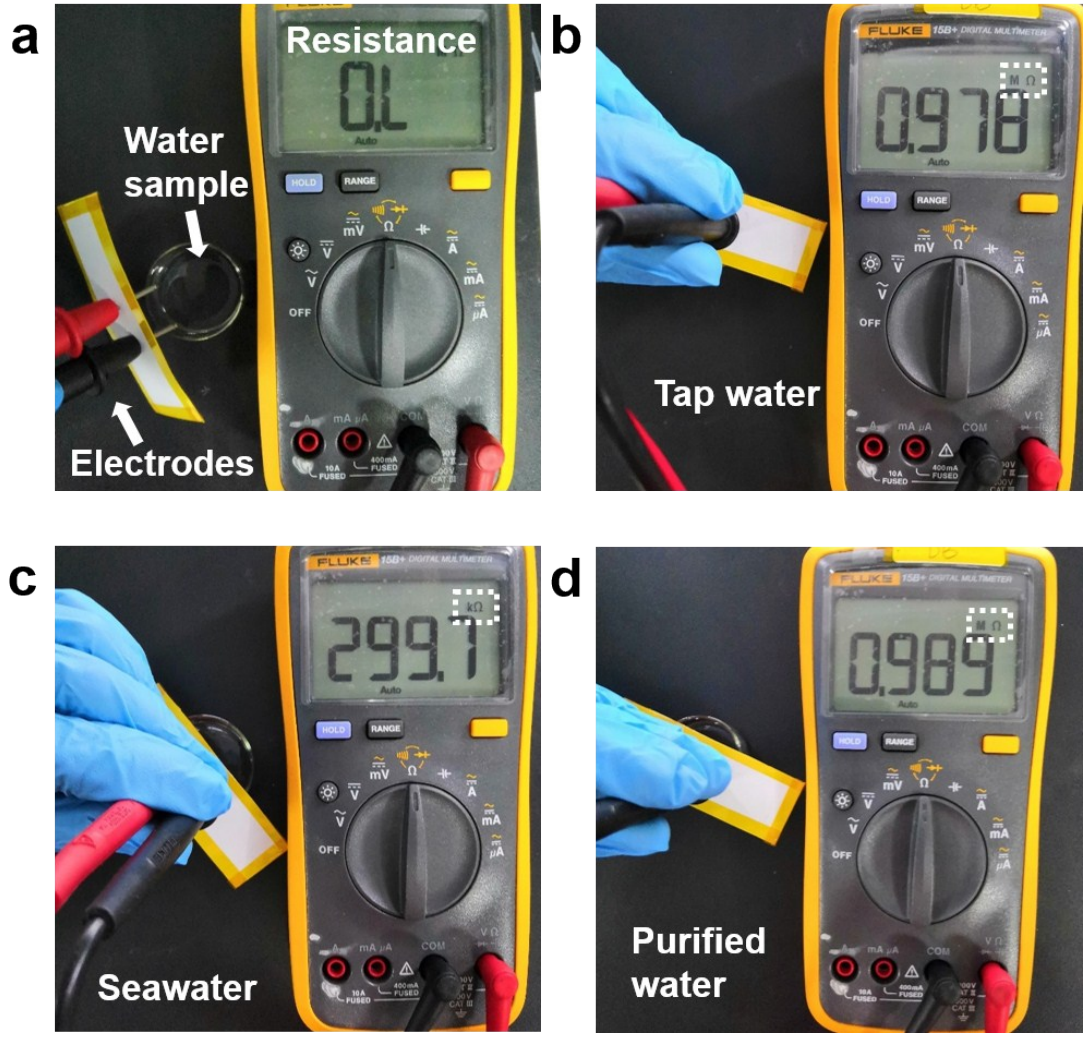

Fig. S7 (a) Experimental setup for the evaluation of water purity by using a multimeter with a constant distance between the two electrodes. The resistance of (b) the tap water, (c) the seawater and (d) the seawater purified by utilizing the solar evaporator indicating the high purity of the purified water.

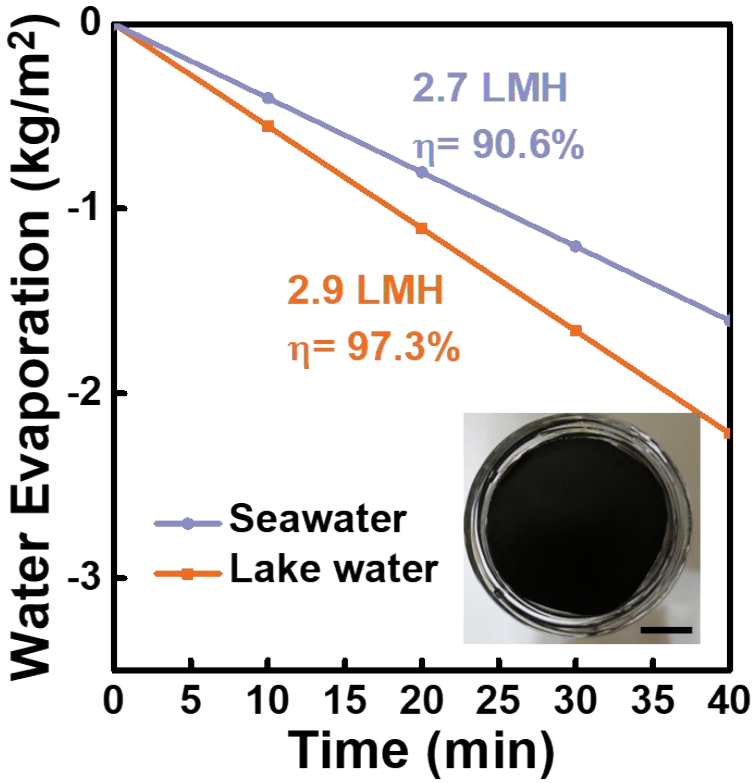

Fig. S8 Water evaporation rate of TiO_2/PPyNP based solar evaporator with similar size to water container under 2 sun irradiation. Inset: CCD image of solar evaporator floating on water surface. The scale bar is 5mm.

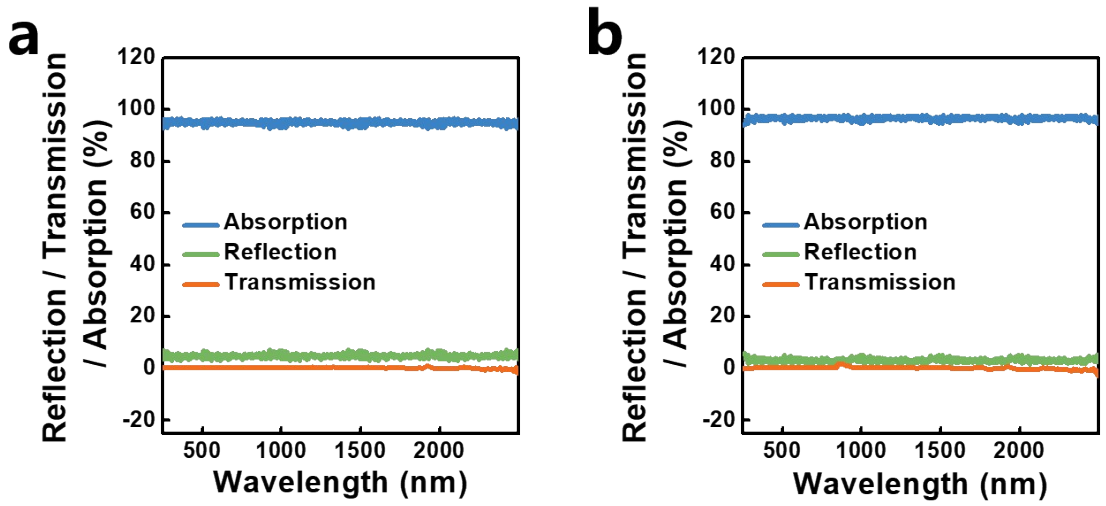

Fig. S9 UV-vis-NIR spectra of the TiO_2/PPyNP based solar evaporators containing (a) 15 wt% (evaporator 1) and (b) 25 wt% (evaporator 3) TiO_2NP content.

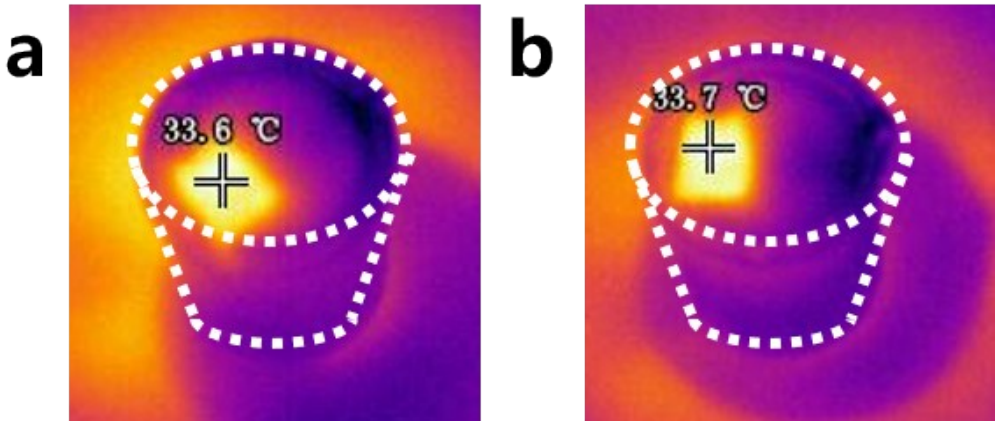

Fig. S10 The thermal imaging showing the equilibrium temperatures of the evaporators during the evaporation process for (a) evaporator 1, and (b) evaporator 3. The slightly higher temperature as compared to that of evaporator 2 shown in Fig. 3a,b is likely due to the low evaporation efficiency which leads to the rise of the evaporator's temperature.

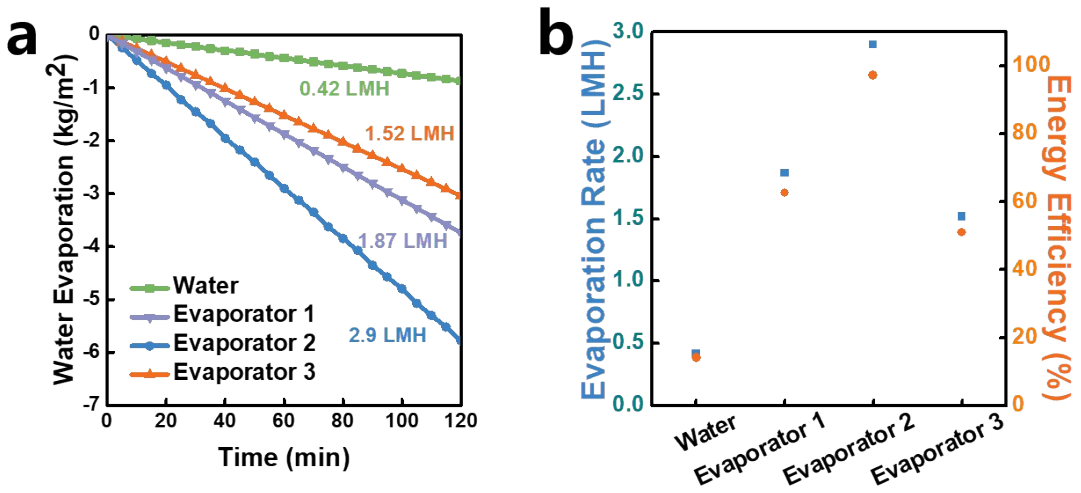

Fig. S11 (a) The water evaporation rates of different evaporators under 2 sun. (b) The energy efficiency and the evaporation rate of different evaporators under 2 sun.

Table S1 The evaporation rates of the TiO_2/PPyNP based solar evaporator with different compositions.

	TiO_2 (wt%)	Water evaporation rate (LMH)	Energy efficiency
No evaporator	0	0.42	14.1%
Evaporator 1	15	1.9	62.7%
Evaporator 2	20	2.9	97.3 %
Evaporator 3	25	1.5	51%

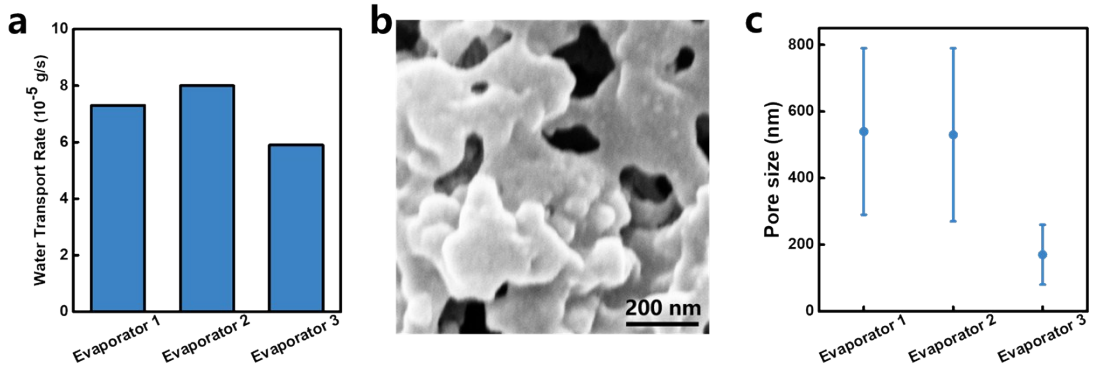

Fig. S12 (a) The water transport rates of different evaporators. (b) SEM image of evaporator 3. (c) The pore sizes of different evaporators.

The best operation temperature

The best operation temperature was evaluated based on the evaporation performance of the TiO_2/PPy based evaporator, which could be tuned by the following two different parameters: (1) the material composition and (2) C_{opt} of solar irradiation.

(1) The material composition:

As can be seen from Fig. S10, the equilibrium temperatures of the evaporators during the evaporation process for a solar evaporator containing 15 wt% TiO_2 (evaporator 1) and 25 wt% TiO_2 (evaporator 3) are 33.6 ˚C and 33.7 ˚C, respectively. The higher value as compared to that of evaporator 2 shown in Fig. 3a (33.2 ˚C) is likely due to the low evaporation efficiency which leads to the rise of the evaporator's temperature. In addition, we have studied the evaporation performance of the TiO_2/PPyNP based solar evaporator with different TiO_2 contents. As can be seen from Table S1, the TiO_2/PPyNP based solar evaporator containing 20 wt% TiO_2 (evaporator 2) exhibits the best evaporation performance and the operation temperature in this case is around 33.2 ˚C.

(2) C_{opt} of solar irradiation：

Under light irradiation with different intensities, the TiO_2/PPyNP based solar evaporator exhibits different temperatures, as shown in the Fig. S6d. Furthermore, we have evaluated the evaporation performance of the TiO_2/PPyNP based solar evaporator under different optical concentration. As can be seen from the Fig. S6b, the solar evaporator achieved the highest energy efficiency under 2 sun irradiation with the best operation temperature being about 33.2 ˚C.

Therefore, in the current work, we utilized the solar evaporator containing 20 wt% TiO_2 which is operated under 2 sun irradiation in order to achieve the best performance and under this condition, the best operation temperature is approximately 33.2 ˚C."

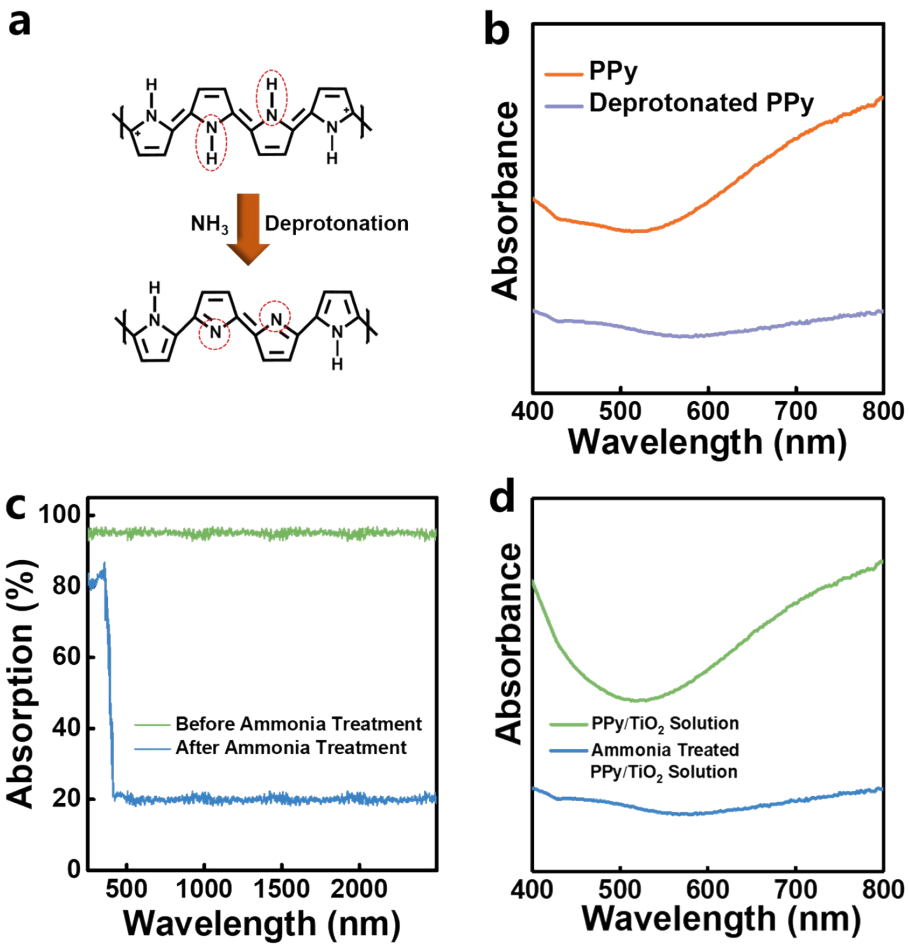

Fig. S13 (a) Deprotonation process of the PPy polymer under the influence of ammonia. (b) The UV-vis spectra of PPy before (red curve) and after (purple curve) deprotonation. (c) UV-vis-NIR spectra of the TiO_2/PPyNP based solar evaporator before (green curve) and after (blue curve) ammonia treatment. (d) UV-vis spectra of the solution containing the TiO_2/PPyNPs before (green curve) and after (blue curve) ammonia treatment.

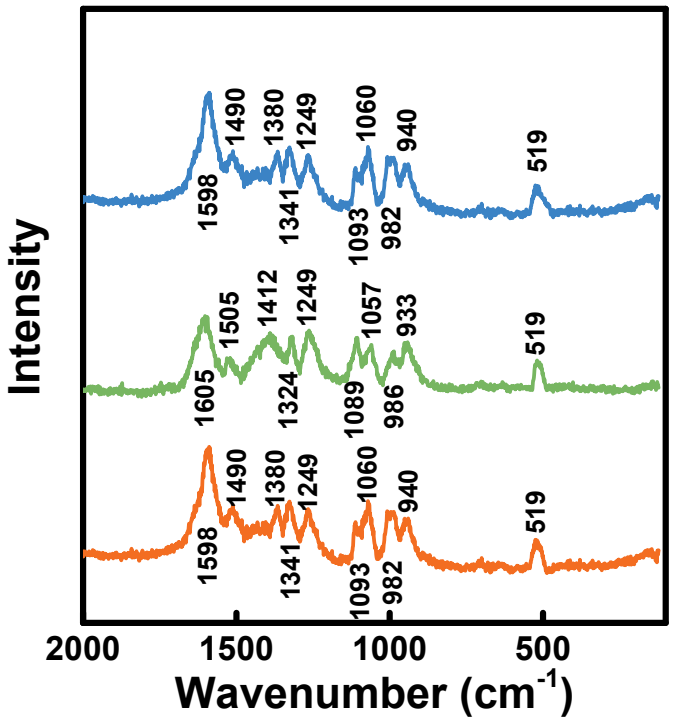

Fig. S14 Raman spectra of the evaporator before (blue curve) and after (green curve) deprotonation with ammonia gas, followed by re-protonation by HCl (orange curve).

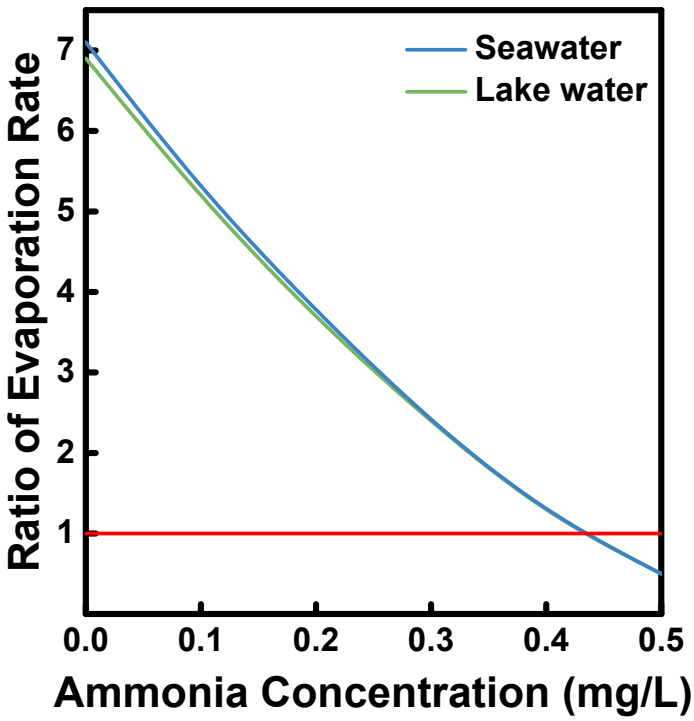

Fig. S15 Ratio of evaporation rates (without or with solar evaporator) of water containing different concentration of ammonia.

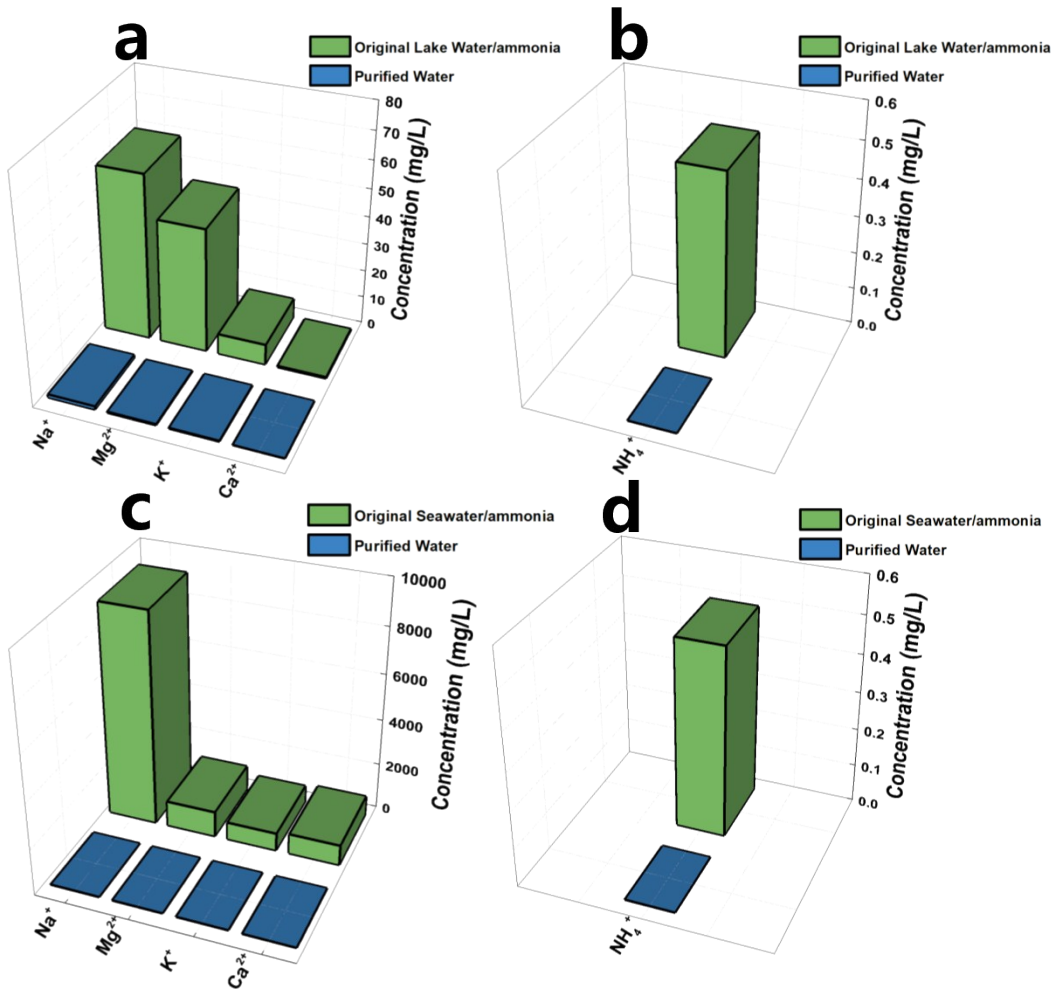

Fig. S16 Composition of water body before (green column) and after (blue column) evaporation from (a,b) lake water/ammonia and (c,d) seawater/ammonia. The original lake water and seawater contains ammonia with a concentration of 0.5 mg/L.

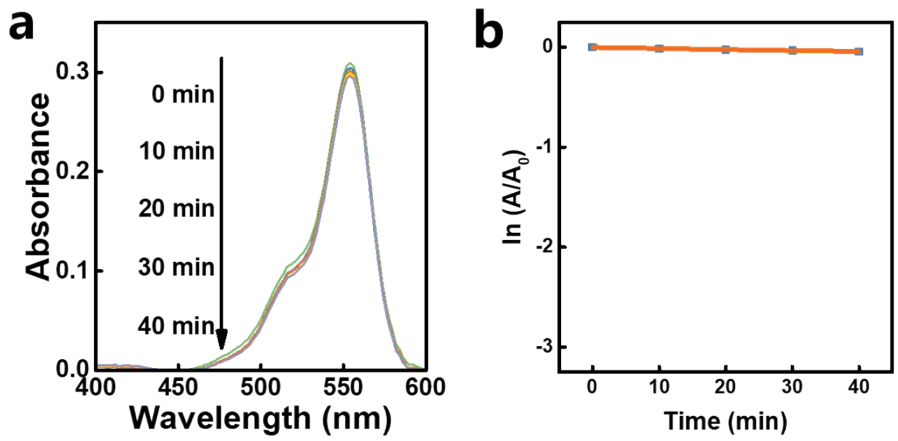

Fig. S17 (a) UV-vis spectra of the degradation of RhB without the solar evaporator at different time interval. (b) The relation of $\ln(A/A_0)$ versus time for the degradation, where A_0 is the original peak absorbance at 552 nm and A is the absorbance at 552 nm for different period of degradation time.

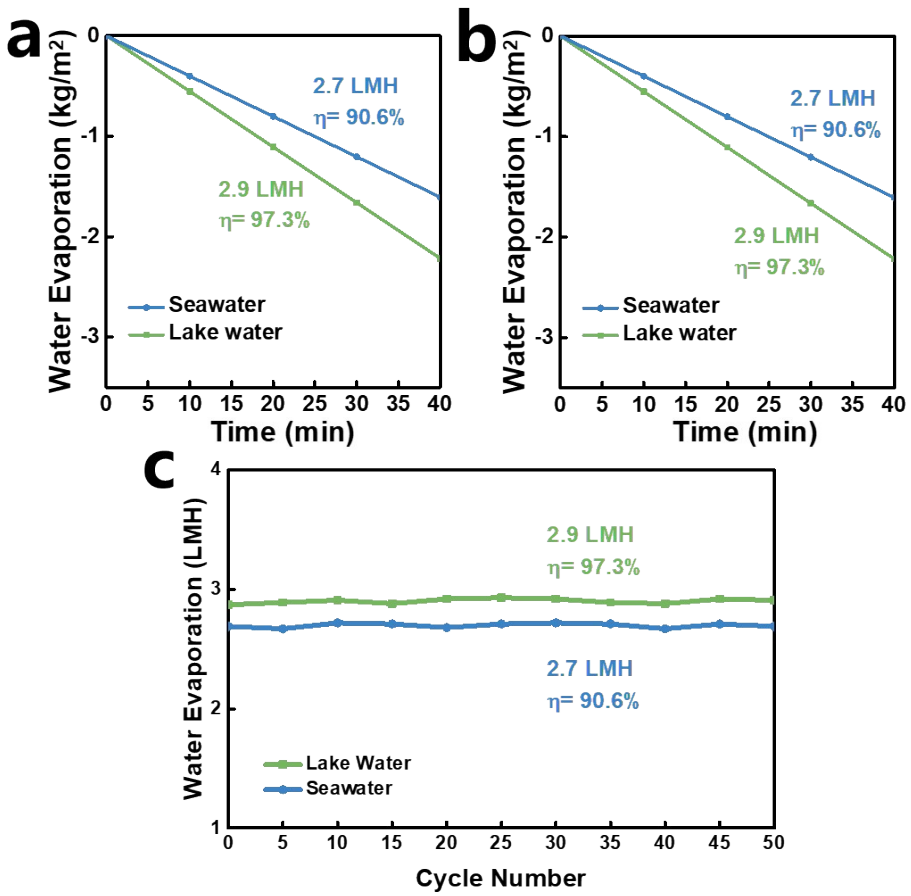

Fig. S18 Under 2 sun irradiation, the water evaporation for lake water and seawater (a) without RhB and (b) with RhB in the presence of solar evaporator. (c) The evaporation performance of the evaporator for 50 cycles (40 min evaporation for each cycle) on lake water (green curve) and sea water (blue curve) which contain RhB.

Table S2 Performance of the reported evaporators under 2 sun irradiation.

Material	Evaporation rate	Energy efficiency	Reference
PVA-PPy cluster	3.8 LMH	>98 %	1
Balsa wood	1.8 LMH	60 %	2
3D Graphene	0.8 LMH	27 %	3
American basswood	2.2 LMH	71 %	4
Aluminum nanoparticle	2.3 LMH	73 %	5
Cu_9S_5/PVDF	2.5 LMH	78 %	6
Poly(1,3,5-hexahydro-1,3,5-triazine)	2.5 LMH	78 %	7
Exfoliated graphite/carbon foam	2 LMH	65 %	8
Indium nanoparticles/microporous membrane	2.7 LMH	82 %	9
Tetrakis (4-carboxyphenyl) porphyrin/Co^{2+}	2.3 LMH	73 %	10

References

1. F. Zhao, X. Zhou, Y. Shi, X. Qian, M. Alexander, X. Zhao, G. Yu, S. Mendez, R. Yang, L. Qu, *Nat. Nanotechnol.*, 2018, **13**, 489-495.

2. S. He, C. Chen, Y. Kuang, R. Mi, Y. Liu, Y. Pei, *Energy Environ. Sci.*, 2019, **12**, 1558-1567.

3. Y. Yang, R. Zhao, T. Zhang, K. Zhao, P. Xiao, Y. Ma, *ACS nano*, 2018, **12**, 829-835.

4. M. Zhu, Y. Li, G. Chen, F. Jiang, Z. Yang, X. Luo, *Adv.Mater.*, 2017, **29**, 1704107.

5. L. Zhou, Y. Tan, J. Wang, W. Xu, Y. Yuan, W. Cai, S. Zhu, *Nat. Photonics*, 2016, **10**, 393.

6. F. Tao, Y. Zhang, K. Yin, S. Cao, X. Chang, Y. Lei, *Sustainable Energy & Fuels*, 2018, **2**, 2762-2769.

7. Q. Chen, Z. Pei, Y. Xu, Z. Li, Y. Yang, Y. Wei, Y. Ji, *Chem. Sci.*, 2018, **9**, 623-628.

8. H. Ghasemi, G. Ni, A. M. Marconnet, J. Loomis, *Nat. Commun.*, 2014, **5**, 4449.

9. L. Zhang, J. Xing, X. Wen, J. Chai, S. Wang, Q. Xiong, *Nanoscale*, 2017, **9**, 12843-

12849.

10. L. Chen, D. Li, Y. Wang, C. Duan, *Nanoscale*, 2019, **11**, 11121-11127.